IOPscience iopscience.iop.org

Home Search Collections Journals About Contact us My IOPscience

Optical, electrical and structural characterization of chloride-doped ZnO nanopillars obtained by electrodeposition

This content has been downloaded from IOPscience. Please scroll down to see the full text.

2016 J. Phys. D: Appl. Phys. 49 215103

(http://iopscience.iop.org/0022-3727/49/21/215103)

View the table of contents for this issue, or go to the journal homepage for more

Download details:

IP Address: 170.210.64.16
This content was downloaded on 04/05/2016 at 18:29

Please note that terms and conditions apply.

IOP Publishing Journal of Physics D: Applied Physics
J. Phys. D: Appl. Phys. **49** (2016) 215103 (10pp) doi:10.1088/0022-3727/49/21/215103

Optical, electrical and structural characterization of chloride-doped ZnO nanopillars obtained by electrodeposition

M Berruet[1], D L Gau[2], E A Dalchiele[2], M Vázquez[1] and R E Marotti[2]

[1] División Electroquímica y Corrosión, INTEMA, Facultad de Ingeniería, CONICET-Universidad Nacional de Mar del Plata, J.B. Justo 4302, B7608FDQ Mar del Plata, Argentina
[2] Instituto de Física and CINQUIFIMA, Facultad de Ingeniería, Universidad de la República, Julio Herrera y Reissig 565, C.C. 30, 11000 Montevideo, Uruguay

E-mail: mberruet@fi.mdp.edu.ar

Received 15 October 2015, revised 8 March 2016
Accepted for publication 14 March 2016
Published 3 May 2016

Abstract

As-grown and chloride-doped ZnO nanopillars were electrodeposited onto bare FTO/glass and ZnO-compact layer/FTO/glass substrates. To analyse the effect of the presence of chloride ions in the electrolytic bath, NH_4Cl was progressively added up to 0.02 mol l^{-1}. As a preliminary examination, the morphology of ZnO nanostructures was analysed by SEM micrographs and chlorine incorporation was detected by EDS. Then, a detailed analysis comprising structural, electrical, optical and defect properties was constructed using XRD, electrical resistance measurements and UV–Vis–IR spectroscopy. As the chlorine concentration in the film increases, XRD reveals a displacement of diffracted planes due to macrostrain of the ZnO lattice and the electrical resistance diminishes. Also, the UV optical absorption edge shifts to higher energies due to the Moss–Burstein effect, which corresponds to electron densities in the order of 1–6 $\times$ 10^{19} cm^{-3}, and the infrared spectra reveal the presence of free electrons, allowing a more precise determination of the free electron densities.

Keywords: zinc oxide, semiconductors, optical properties, Brazilian MRS

(Some figures may appear in colour only in the online journal)

1. Introduction

ZnO is a semiconductor that has awakened the interest of researchers for many decades. In terms of characterization, reports go back to 1935 or even earlier [1]. The special interest in ZnO has arisen because of its strong potential for many applications, like short-wavelength optoelectronic devices, among many others [2]. Moreover, when compared to other semiconductors with similar physical properties, like GaN [3], ZnO has a simple crystal-growth technology, resulting in a potentially lower cost for ZnO-based technologies.

ZnO usually behaves as an n-type semiconductor due to native defects [4]. However, the electrical and optical properties can be tuned due to the ability of ZnO to accept different types of impurities. Yet, n-type doping is relatively easier than p-type doping. Within the n-type doping group, the literature shows that much attention has been paid to cationic doping as substitutional elements for Zn [5–7] whereas anionic doping as substitutional elements for O is more recent [8–10].

On the other hand, the potential application of nanomaterials depends on the shape of the nanostructure. For example, ordered and nanostructured semiconductors are specially studied due to their performance in response to photon capturing and/or photocarrier collection [1]. For instance, in third-generation solar cells the most important parameters influencing the solar cell efficiency are the length, diameter and density of nanorods [11]. High donor impurities concentration and ordered nanostructures of ZnO can be properly combined to create an anti-reflective layer for effective light trapping in thin-film solar cells [12]. Such highly doped nanostructures can be obtained by controlling the reaction conditions during heterogeneous deposition from

 © 2016 IOP Publishing Ltd Printed in the UK

the electrochemical route. In potentiostatic electrodeposition, the reaction mechanism that governs ZnO formation and morphology is strongly dependent on the electrochemically active precursors [10, 13].

Some authors have reported the growth of ZnO rods by electrodeposition using zinc nitrate as a precursor of oxygen and zinc simultaneously, but adding hexamethylenetetramine ($C_6H_{12}N_4$) as a stabilizer and alternative precursors of OH^- ions [14, 15]. However, in the present work, the deposition of Cl-doped nanopillars of ZnO (NP-ZnO) has been possible without putting any additive into the solution. The aim of this work is to study the influence of the NH_4Cl concentration on the structural, optical and electrical properties of the electrodeposited ZnO nanopillar arrays.

2. Material and methods

2.1. Substrate

Glass coated with a transparent conducting tin oxide FTO (Zhuhai Kaivo Electronic Components Co., Ltd.) was used as the substrate. The substrate was cut into rectangular pieces resulting in an exposed area of $1 \times 3\,cm^2$. Prior to use, the substrates were degreased with detergent solution and then rinsed in an ultrasonic bath during 10 min, first with acetone and then with ethanol.

2.2. ZnO electrodeposition

Electrodepositions were carried out using a Voltalab PGP 201 potentiostat and a standard three-electrode cell configuration. A saturated calomel electrode (SCE) was used as reference and a Zn foil as counter electrode. The electrolytic bath consisted of aqueous solutions of 10 mmol l^{-1} $Zn(NO_3)_2$. NP-ZnO was deposited at 70 °C with constant stirring and holding the electrode at −1 V versus SCE up to a final charge density of 1.33 °C cm^{-2}.

In order to incorporate chloride in the structure, NH_4Cl was progressively added in concentrations of 0, 5, 10 and 20 mmol l^{-1}. Then, the molar contents of chloride will be expressed and referenced using the ratio between Cl^- and Zn^{2+} in the precursor solutions, i.e. $Cl^-/Zn^{2+} = 0$, 0.5, 1 and 2 and samples will be labelled as ED0, ED0.5, ED1 and ED2, respectively.

For the electrical properties characterization, such as electrical resistance, a compact layer of ZnO (SP-ZnO) was deposited previous to the nanopillars. The method was described in detail by O´Regan *et al* [16], and has been used by other authors [17]. The spraying process consisted of 15 cycles. In such conditions, the samples were renamed as SP-ED0, SP-ED0.5, SP-ED1 and SP-ED2. This series of samples was also used for the optical characterization.

2.3. Characterization

The films were analysed by x-ray diffraction (XRD) using a PANalytical X'Pert Pro diffractometer, Cu-K alpha radiation at 40 kV and 40 mA. The samples were scanned using grazing incidence, between 20° and 80° at 0.02° s^{-1}. The crystallographic data were taken from the literature and analysed with X'Pert HighScore software.

The morphology of the layers was studied by scanning electron microscopy (SEM), using a JEOL JSM-6460LV microscope. The composition was analysed by x-ray energy dispersive spectroscopy (EDS). The system used was an EDAX Genesis XM4-Sys 60, equipped with a Multichannel Analyzer EDAX mod EDAM IV, Sapphire Si(Li) detector and Super Ultra Thin Window of Be, and EDAX Genesis software.

The particular morphology of the nanopillar arrays makes their electrical characterization difficult. Two methods were used to guarantee the results. Sheet resistance, for samples grown onto a spray pyrolysis (SP) compact layer, were characterized using a homebuilt four-point probe set-up [18], a Keithley 6221 current source (in DC mode) and a Keithley 2182A Nanovoltmeter. The sheet resistance of the conductive FTO layer was considered as a parallel sheet resistance to the one of the ZnO layer under study [19]. At least ten points were measured, obtaining linear voltage versus current curves. The sheet resistance could be calculated from their slope. For the rest of the samples (those without SP compact layer) a one-point probe configuration was used, with the Au probe as the positive contact onto the ZnO and the FTO film as the negative contact. Thus, in forward bias, Au is at a higher voltage relative to the FTO. Voltage versus current curves with Schottky-like non-ohmic behaviour, were obtained by applying a voltage sweep in the range between −2 and 3 V. The Schottky junction was obtained by carefully touching the ZnO with an Au point until a signal was detected. A Teq-04 potentiostat was employed to carry out these measurements and the resistance of the whole sample was obtained from the high current slope.

The optical properties in the visible and UV region were studied using an experimental set-up that consisted mainly in an ORIEL 77250 monochromator with an ORIEL 77298 diffraction grating. The light source from a Xe lamp (ORIEL 6271) was chopped with an SRS SR540 chopper. The light (transmitted or reflected from the sample) was detected with an UDT 11-09-001-1 (100 mm^2 wide area UV-enhanced unbiased silicon detector). A first lock-in amplifier (SRS SR530) extracted the signal from this detector while a second (EG&G 5209) monitored light source intensity fluctuations. The transmittance was measured for all the samples using the lamp spectrum as a reference. This is done to avoid spurious effects that originated in the interference pattern already present in the FTO/glass substrate [20]. For those samples grown onto a SP compact layer, reflectance was also measured. In this case, the diffused light was detected normal to the surface, while illuminated at quasi-normal incidence [21, 22]. In the infrared region (from 1.3 to 25 μm) the reflectance was measured using a Shimadzu IR Prestige-21 Fourier Transform Infrared Spectrometer equipped with an SRM-8000A accessory. Moreover, the interference oscillations observed in the near infrared (1000–3000 nm) were also measured (either by reflectance or transmittance) with the same experimental set-up used for visible and UV but with a tungsten lamp as light source, an ORIEL 77300 diffraction grating and a Sciencetech InAs thermocooled detector. The reference used in the infrared for reflectance measurements was a pure Al

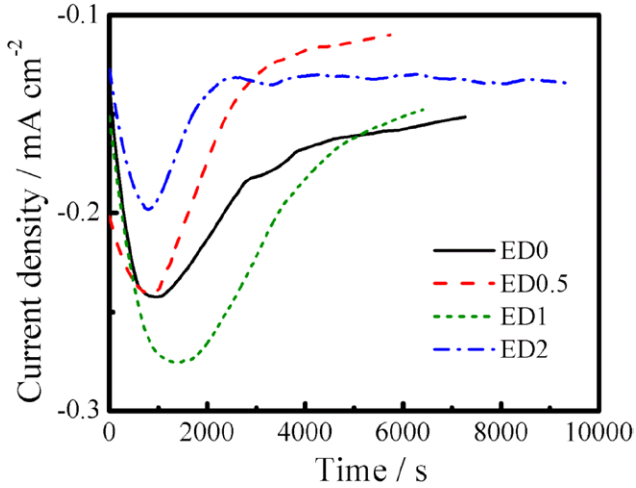

Figure 1. Chronoamperometric curves for NP-ZnO electrodeposited at different Cl^-/Zn^{2+} ratios: ED0 (full line), ED0.5 (dashed line), ED1 (short dashed line) and ED2 (dash dotted line).

mirror, while for transmittance the FTO/glass substrate was used (due to its reduced transmittance in this region). All measurements were performed at room temperature.

3. Results and discussion

In general, chronoamperograms obtained from potentiostatic deposition curves can offer information about growth mechanisms including the type of morphology. In figure 1 chronoamperograms are shown for NP-ZnO electrodeposited using different Cl^-/Zn^{2+} ratios. Taking into account absolute values, the four curves present similarities: an increase in current density to a maximum value after which they begin to decrease to achieve a stationary current. Such behaviour is typical of a diffusion-limited growth mechanism [23]. However, it has been observed that the differences in the plateau values do not show clear correlations. Possible reasons can be uncontrolled variations in the hydrodynamic regime, uncertainties in substrate areas or differences in the conductivity and morphology of the nanopillars.

The morphology of the nanopillars grown onto FTO can be seen in figure 2. At low magnifications, there seems to be no substantial differences between them, except for ED2. However, at higher magnifications the diameters and the degree of orientation can distinguish them. As observed before by Cui *et al* [23], the diameter increases with the chloride content from about 200 nm for ED0 to values as high as 800 nm for ED2. Moreover, the degree of verticality diminishes [17]. For the SP-ED samples (results not shown) the morphology is almost unchanged with the Cl^-/Zn^{2+} ratios and the diameters remain between 125–200 nm, confirming the role of the compact layer. In fact, Elias *et al* [17] have shown that ZnO nanowire arrays grown on seed layers present an increase (up to a factor 6×) of the nanowire array density in comparison to those obtained directly on naked substrates. Smaller densities usually allow thicker nanopillars and a less aligned array [23].

The elemental composition of the nanopillars in atomic percentage was further explored by EDS as shown in table 1, where the Cl/Zn content ratios are compared. As can be seen, the chlorine content in the nanopillars increases with the chloride concentration in the solution. The total amount of chlorine detected can include chloride ions adsorbed onto the nanopillar surface or located into the bulk. To minimize adsorption, the samples were vigorously rinsed in water.

Figure 3 shows XRD patterns of ZnO nanopillars deposited onto FTO at different Cl^-/Zn^{+2} ratios. Only the three main peaks are shown. The unidentified peaks correspond to the FTO substrate and to satellite signals of ZnO with K_β radiation. Except for ED2, the diffractograms can be interpreted in terms of a hexagonal structure matching that of wurtzite (PDF 79-0207) with preferential orientation along the *c* axis. The intensity has been normalised with respect to the (1 0 1) plane to visualize the ratios between the relative intensities of plane (0 0 2) and (1 0 1), i.e. $I_{max}^{(002)}/I_{max}^{(101)}$. There is a noticeable correlation between these relations of intensities and the disorder of the nanopillars (verticality or orientation degree [17]). Figure 2 showed a growth perpendicular to the substrate that has been confirmed by the preferential orientation of the (0 0 2) plane in figure 3. However, as the chloride concentration increases, the relation $I_{max}^{(002)}/I_{max}^{(101)}$ decreases, indicating a degree of disorder or non-alignment of the nanopillars that can be seen in figure 2. Two additional parameters evaluated from XRD are the displacement of diffracted planes and peak broadening in the (0 0 2) plane of NP-ZnO grown in the presence of chloride, compared to NP-ZnO grown in the absence of chloride (ED0). The insert of figure 3 shows patterns of each sample in the (1 0 1) plane where the displacement is clearly observed. This shifting to lower angles when higher amounts of ammonium chloride are incorporated has been observed by various authors [15, 23], and has been attributed to an expansion, or macrostrain of the ZnO lattice due to the replacement of O^{2-} ions (1.32 Å) with the larger Cl^- ones (1.81 Å) [24]. Such chloride impurities may act as electrical donors if they substitute oxygen atoms or they may present acceptor behaviour if they are in an interstitial position. The broadening of the (0 0 2) peak increases as chloride is incorporated into the structure, as shown in table 1. The corresponding crystallite size calculated by Scherrer's equation [24] was in all cases larger than 45 nm. For other planes no correlation was found.

Electrical properties such as sheet resistance or eventually resistance of each sample have been estimated as described in detail in section 2.3. However, both methods have limitations for 1D nanostructured materials such as nanopillars, nanorods or nanowires. For example, in order to obtain sheet resistance using four-point probes each layer must be a compact, homogenous and thin. Moreover, when there are two or more layers it is not possible to accurately know the contribution of each layer. Even if those considerations are taken into account, the measurements can always be compared among each method. Electrical resistance (R) values for ED samples and sheet resistance (R_s) values for SP-ED samples are shown in table 1. In spite of changes in morphology (not shown) of the nanopillars grown onto different substrates (FTO and SP-ZnO/FTO), for the two series of electrodeposited nanopillars, R and R_s decrease as chloride is incorporated into the precursor solution, giving a direct correlation between free

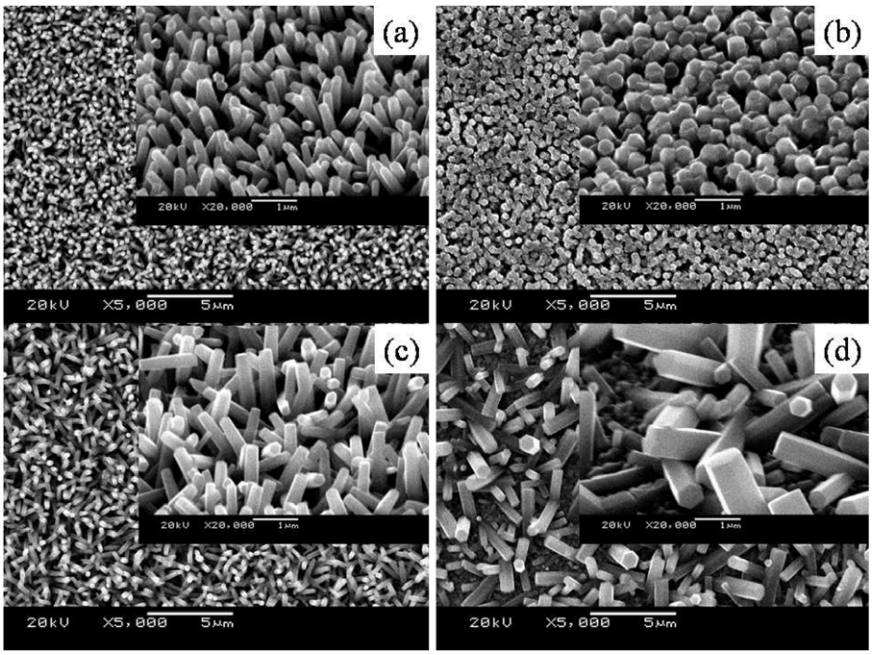

Figure 2. SEM micrographs of the nanopillars grown onto FTO: frontal view for samples (a) ED0, (b) ED0.5, (c) ED1 and (d) ED2. Insets correspond to higher magnification of the lateral view at 45° inclination.

Table 1. Cl/Zn content by EDS, (0 0 2) plane broadening and electrical resistance of nanopillars grown onto FTO and SP-ZnO/FTO substrates.

Sample	Cl^-/Zn^{2+} in solution	Cl/Zn by EDS	FWHM (rad) $\times 10^{-4}$	R (Ω)	R_s (Ω sq^{-1})
ED0	0	0.008	47	69 ± 2	—
ED0.5	0.5	0.015	48	54 ± 5	—
ED1	1	0.014	51	49 ± 5	—
ED2	2	0.024	58	41 ± 3	—
SP	—	—	—	—	553
SP-ED0	0	0.008	—	—	82
SP-ED0.5	0.5	0.016	—	—	20
SP-ED1	1	0.021	—	—	106
SP-ED2	2	0.020	—	—	14

carrier and chloride concentrations. An exception can be seen for SP-ED1 for which *Rs* is between SP and SP-ED0. The reason may be that the diameters of the nanopillars grown onto the SP layer (not shown) are similar to the nuclei diameter of the SP layer.

Figure 4 shows the optical transmittance (T) of the samples grown onto FTO/glass substrate (ED, figure 4(a)) and onto the SP compact layer (SP-ED, figure 4(b)). The latter includes the spectra of the bare FTO/glass substrate and of ZnO deposited by SP. All the samples with electrodeposited ZnO have similar spectra with a sharp increase in the UV region (close to 350–375 nm) and a smoother increase of the transmittance from the blue part of the visible region to the infrared region. The first structure corresponds to the ZnO absorption edge, while the second may be due to light scattering [25]. In effect, this light scattering is responsible for the white 'milky' appearance of the sample by reflectance and explains the orange colour many samples have when looking

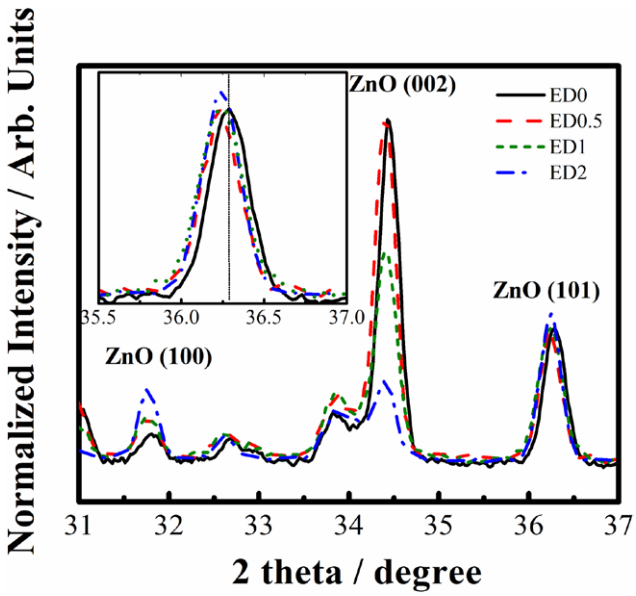

Figure 3. Grazing incidence—XRD patterns for samples ED0 (full line), ED0.5 (dashed line), ED1 (short dashed line) and ED2 (dash dotted line). The insert corresponds to magnification of the (1 0 1) planes.

at a white light through them [26]. The former structure is not present in the FTO/glass substrate (see figure 4(b)), and is very sharp in the SP sample. For this case, even a relative transmittance minimum (absorptance maximum) can be seen for wavelengths just below the absorption edge. This structure is typically observed in undoped nanometric ZnO films and may correspond to excitonic absorptance [27, 28]. It can also be noted that close to 700 nm the SP sample has a higher transmittance than the FTO/glass substrate. For this reason and to avoid transmittance values artificially higher than 100%, the lamp spectrum was used as reference [10, 29].

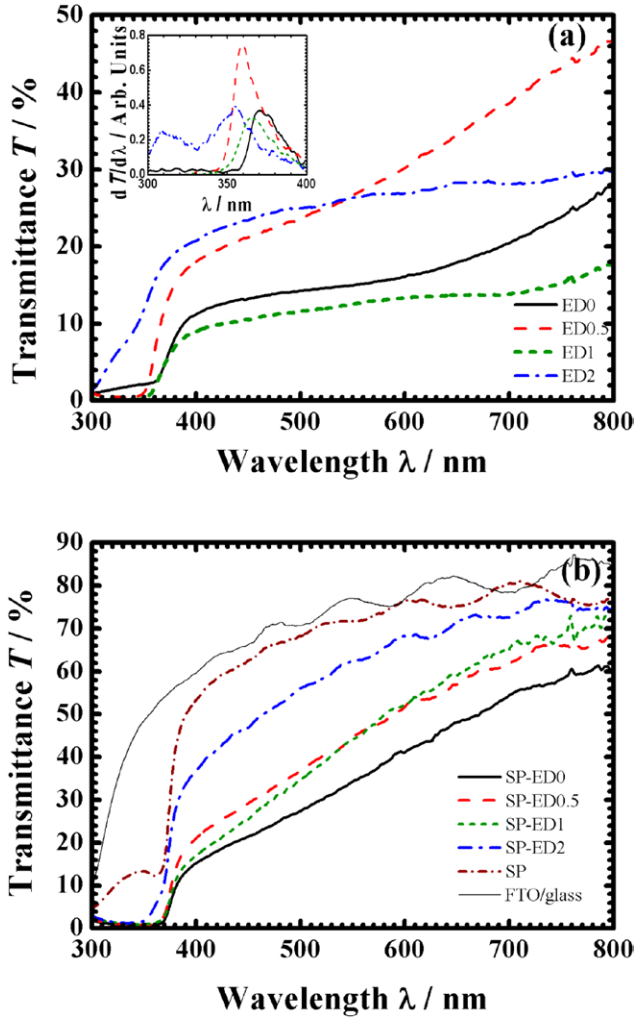

Figure 4. Transmittance spectra for samples: (a) ED0 (full line), ED0.5 (dashed line), ED1 (short dashed line) and ED2 (dash dotted line). Inset shows transmittance T first derivative against wavelength λ. (b) For samples SP-ED0 (thick full line), SP-ED0.5 (dashed line), SP-ED1 (short dashed line), SP-ED2 (dash dotted line), SP (short dash dotted line) and FTO/glass substrate (thin full line).

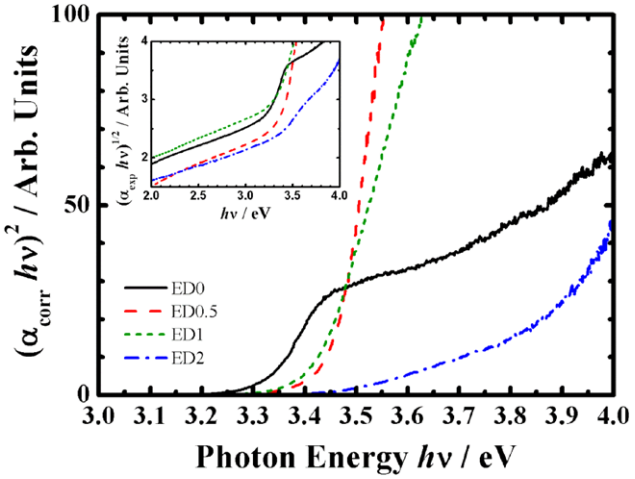

Figure 5. Plots for direct bandgap energy (E_g) determination for samples of ED series: ED0 (thick full line), ED0.5 (dashed line), ED1 (short dashed line) and ED2 (dash dotted line). α_{corr} is the corrected absorptance after subtracting a background absorptance obtained from a linear fitting in the below E_g part of the Tauc plots of the inset.

The bandgap energy (E_g) may be obtained from the absorption edge position. Figure 4 shows a shift of this edge as the ratio Cl^-/Zn^{2+} increases (figure 4(a) ED samples, figure 4(b) SP-ED samples). Although this shift may be not monotonic it can be clearly seen from the peak position of the first derivative of the transmittance T against wavelength λ (figure 4(a) inset). It goes from 372 nm (~3.33 eV) for ED0 to 355 nm (3.49 eV) for ED2. The shift is smaller in the case of the samples of figure 4(b): from 375 nm (~3.30 eV) for SP-ED0 to 373 nm (~3.32 eV) for SP-ED2. The obtained values are in good agreement with the results reported by Tena-Zaera *et al* for Cl-doped ZnO nanowires [30], which are in the range from 3.32–3.34 eV. A similar tendency has also been reported by Cui *et al* [23] from photoluminescence measurements.

The optical properties of NP-ZnO, mainly the values of transmittance and reflectance in the transparency region, are strongly influenced by light scattering. The general morphology of the NP-ZnO, i.e. diameter, length, density and order (or verticality of the NP-ZnO) is determinant in the nature of light scattering [31]. The dependence of the scattered light with these parameters has already been studied by several authors [11, 31–34]. However, as the multiple scattering present is a very complex phenomenon, no simple dependence can be obtained. Therefore, the following procedure was used for a better determination of the E_g values from the extrapolation to the zero absorption of a linear fitting in $(\alpha h\nu)^2$ against photon energy $h\nu$, where α is the absorption coefficient [35–37]. First, an experimental absorptance $\alpha_{exp} = -\ln T$ was obtained. Then, a corrected absorptance $\alpha_{corr} = \alpha_{exp} - \alpha_{back}$ was calculated, where the background absorptance α_{back} corrects for zero absorption. The α_{back} dependence with $h\nu$ is obtained from a linear fitting in the below gap region of the Tauc plot, where $(\alpha_{exp}h\nu)^{1/2}$ is plotted against $h\nu$ (as indirect absorption edge) [37, 38]. Figure 5 shows the $(\alpha_{corr}h\nu)^2$ against $h\nu$ plots, while its inset shows the $(\alpha_{exp}h\nu)^{1/2}$ against $h\nu$. In both plots there are clear linear regions.

The procedure of finding α_{back} has already been used in similar nanostructured samples [25, 26, 39], although no real indirect gap is responsible for the α_{back} correction in the present samples. The correction is originated in the fact that the previously mentioned light scattering introduces uncertainty in the zero absorption line, which greatly influences the E_g values [25, 26]. The almost constant value of the transmittance for longer wavelengths (see figure 4(a)) makes a smooth dependence of α_{exp} with $h\nu$, appropriated for this background absorptance. In fact, for the present samples, another background subtraction method was tested, obtaining the background absorption from a linear fitting (in the same spectral region) in a ln α_{exp} against ln λ plot. The E_g values obtained by either method agree within 10 meV, in each case for all samples.

Figure 5 also shows that samples ED0.5 and ED1 have a steep increase in the α_{corr} close to the absorption edge (3.3–3.5 eV). This is because these samples have a transmittance that approaches zero for wavelengths shorter than the one of

Table 2. (a) E_g values obtained from figure 5, electron densities n_1 and Urbach parameter E_{01} obtained from equation (3). Mean plasma frequency ω_p, damping rate γ and corresponding free electron density n_3 obtained from equation (7). (b) E_{g2} values obtained from figure 6 with SP/FTO substrate as reference in reflectance. Electron densities n_2 and Urbach parameter E_{02} obtained from equation (4).

(a)

Sample	E_g (eV)	n_1 (cm^{-3}) $\times 10^{19}$	E_{01} (meV)	ω_p (s^{-1}) $\times 10^{14}$	γ (s^{-1}) $\times 10^{14}$	n_3 (cm^{-3}) $\times 10^{19}$
ED0	3.34 ± 0.02	—	86	3.3 ± 0.1	2.0 ± 0.1	3.7 ± 0.6
ED0.5	3.44 ± 0.01	1.2 ± 0.2	92	4.1 ± 0.1	2.4 ± 0.1	5.9 ± 0.8
ED1	3.42 ± 0.03	0.8 ± 0.5	81	3.3 ± 0.3	2.8 ± 0.1	3.9 ± 1.5
ED2	3.49 ± 0.01	2.1 ± 0.2	205	4.6 ± 0.4	7.1 ± 0.9	7.3 ± 2.3
SP	3.29 ± 0.01	0.2	—	—	—	—
SP-ED0	3.26 ± 0.01	—	—	3.6 ± 0.1	2.2 ± 0.2	4.6 ± 0.6
SP-ED0.5	3.27 ± 0.01	<0.1	—	3.8 ± 0.1	2.3 ± 0.1	5.1 ± 0.7
SP-ED1	3.27 ± 0.01	<0.1	—	4.1 ± 0.1	2.5 ± 0.1	6.0 ± 0.9
SP-ED2	3.30 ± 0.01	0.3	—	4.6 ± 0.3	3.2 ± 0.1	7.4 ± 1.7

(b)

Sample	E_{g2} (eV)	n_2 (cm^{-3}) $\times 10^{19}$	E_{02} (meV)
ED0	—	0.3 ± 0.2	69
ED0.5	—	1.9 ± 0.2	83
ED1	—	1.5 ± 0.7	75
ED2	—	5.8 ± 0.6	165
SP-ED0	3.27 ± 0.01	—	—
SP-ED0.5	3.28 ± 0.01	<0.1	—
SP-ED1	3.29 ± 0.01	0.1	—
SP-ED2	3.31 ± 0.01	0.3	—

the absorption edge (see figure 4(a)). It is directly related to the fact that there are fewer empty spaces in these nanostructures, as seen in the SEM micrograph of figure 2. Meanwhile, the other two samples ED0 and ED2, do not have a null transmittance in the shorter wavelength region. Instead, they show a slight increase in α_{corr} and another absorption edge close to 3.9 eV (see figure 5). This is due to the FTO/glass substrate. More precisely for ED2, both the transmittance and its derivative show the presence of two absorption edges, one close to 350 nm and the other close to 310 nm. The first is due to ZnO while the second is already present in the substrate (see the thin line in figure 4(b)). The substrates may be seen in the transmittance of this sample because, as also shown in the SEM micrograph (figure 2), there are much larger empty regions in between the ZnO nanostructures.

The E_g values obtained from the linear fittings are shown in table 2(a). They correspond to the mean values obtained from different samples grown in the same conditions, while the uncertainties were calculated to include all the values obtained in the corresponding interval. The general trend is that these E_g values increase with the Cl^-/Zn^{2+} ratio, as previously observed. The only exception is ED1 that showed the largest dispersion. The crystal size obtained by the Scherrer equation from the XRD peak broadening is always higher than 45 nm. As this value is much larger than the ZnO exciton Bohr radius (∼1.8 nm) [24], no quantum size effect is expected in the E_g value. So, the shift in the absorption edge with Cl^-/Zn^{2+} may be due to band-filling effects (and eventual bandgap renormalization) originated in excess free electrons due to doping, i.e. the Moss–Burstein effect [40, 41]. In fact, these shifts are comparable to those observed by other authors [10], and assigned to this effect, although theoretical calculations have predicted shifts smaller than 100 meV (∼40 meV for 1% Cl incorporation) [42].

The same procedure was applied to the samples electrodeposited on top of the SP compact layer of ZnO, i.e. the SP-ED series. E_g calculated for each one is, within less than 10 meV, close to the value obtained for the SP sample, which is 3.29 eV as can be seen in table 2(a). This is because this sprayed layer acts as an almost opaque film for the one electrodeposited onto it and the transmittance depends mainly on its absorption edge. Thus, the reflectance R in a diffuse quasi-normal configuration was measured, with light reaching the samples from the side of the electrodeposited NP-ZnO. In this configuration, light interacts more strongly with the NP-ZnO and the measurements should be less sensitive to the properties of the FTO/glass substrate or the SP compact layer. The spectra are shown in figure 6. The inset shows the reflectance first derivative $dR/d\lambda$ against wavelength λ. This peak is smaller and wider for the SP sample, because its reflectance is smoother. In fact, the electrodeposited samples scatter the light more strongly.The peak of $dR/d\lambda$ should follow the shift observed for E_g [22, 43, 44]. The values obtained are shown in table 2(b) as E_{g2}, where the SP/FTO sample was used as reference (spectra not shown). It can be seen that E_{g2} increases with the the Cl^-/Zn^{2+} ratio. E_g values and the shifts are smaller

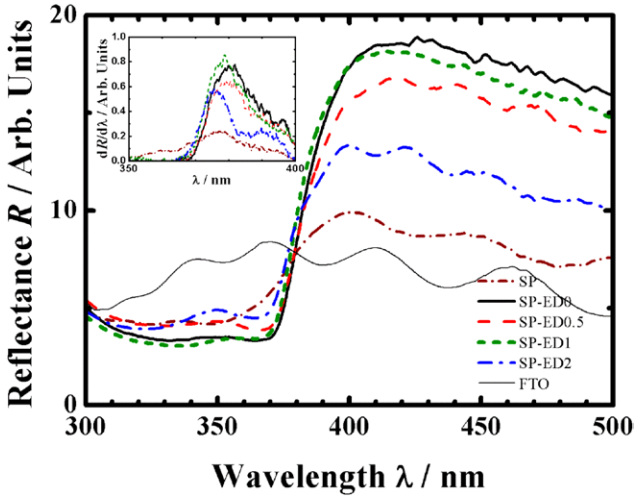

Figure 6. Reflectance spectra (in diffuse quasi-normal configuration) for the samples of the SP-ED series: SP-ED0 (thick full line), SP-ED0.5 (dashed line), SP-ED1 (short dashed line), SP-ED2 (dash dotted line), SP (short dash dotted line) and FTO/glass substrate (thin line). Inset shows its first derivative against λ (except for the FTO/glass substrate).

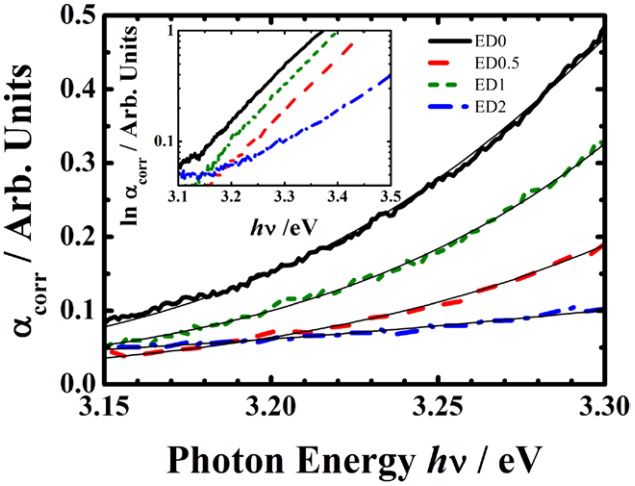

Figure 7. Below gap absorption and Urbach tail determination for samples ED0 (thick full line), ED0.5 (dashed line), ED1 (short dashed line) and ED2 (dash dotted line). Inset shows the same data in ln scale against photon energy $h\nu$.

than the ones found for the ED series, which is a consequence of the measurement procedure [21, 43]. However, they reproduce the general tendency.

The electron densities n corresponding to those absorption edge shifts are calculated using the simple band-filling model [45, 46]:

$$\Delta E_{\mathrm{MB}} = \frac{h^2}{8m_{\mathrm{r}}}\left(\frac{3n}{\pi}\right)^{2/3} \tag{1}$$

where $\Delta E_{\mathrm{MB}} = E_{\mathrm{g}}(n) - E_{\mathrm{g}}(0)$ is the energy shift being $E_{\mathrm{g}}(n)$ the absorption edge position for an electron concentration n, and $E_{\mathrm{g}}(0)$ is the actual bandgap energy, i.e. no conduction electrons, h is the Planck constant and m_{r} is the reduced mass $m_{\mathrm{r}} = (1/m_{\mathrm{e}} + 1/m_{\mathrm{h}})^{-1}$, with m_{e} (m_{h}) the electron (hole) effective mass. The values of $m_{\mathrm{e}} = 0.275\, m_0$ [47] and $m_{\mathrm{h}} = 0.59\, m_0$ [48] were used. The values of n_1 in table 2(a) were obtained from equation (1) where the measured E_{g} for samples ED0 and SP-ED0 were used as $E_{\mathrm{g}}(0)$, respectively. These values of n_1 do not include bandgap shrinkage due to renormalization many-body effects [36, 49]. A phenomenological equation that includes this correction is [49, 50]:

$$\Delta E_{\mathrm{g}} = \Delta E_{\mathrm{MB}} - B\left(\frac{n-n'}{n'}\right)^{\gamma} \tag{2}$$

where ΔE_{MB} is the correction obtained by equation (1), $B = 75$ meV, $n' = 2 \times 10^{19}$ cm^{-3} and $\gamma = 0.55$ [49]. The correction should be included for densities $n > n'$ (onset of bandgap shrinkage). Thus, for the obtained values of n_1 in table 2(a) the correction would be necessary just for the highest density (sample ED2). But still the onset is within the uncertainty region of this value, therefore no further improvement may be necessary. The values of n_2 in table 2(b) where obtained from equation (2) considering now that the $E_{\mathrm{g}}(0)$ $\sim$3.30 eV, i.e. the same value obtained for the SP compact layer. Once again the correction is necessary just for the highest doped sample, although in this case it is relatively important. As can be seen from table 2, as the ΔE_{g} is smaller, the densities are also smaller and the bandgap shrinkage correction of equation (2) is not necessary in any case.

Figure 7 shows the α_{corr} against $h\nu$ spectra for the ED series, in the below gap region. This absorption follows an exponential shape known as Urbach's rule [51]:

$$\alpha = \alpha_0 \exp\left(\frac{h\nu}{E_0}\right) \tag{3}$$

where E_0 is the band tail (or Urbach's parameter) [21] and α_0 is a constant absorption, independent of photon energy. E_0 measures the region where the band tail extends; it is an empirical energy 'broadening' parameter [35, 52] that can be used as a measurement of lattice distortion originated by defects present in the material. The E_{01} values in table 2(a) were obtained from the slope of the plot ln α_{corr} against $h\nu$ (see figure 7 inset). As these values may be greatly influenced by the signal-to-noise ratio of the measurements and the energy region of the fitting, another approach for obtaining the Urbach's parameter was also used. It is based on using a sigmoidal curve for the α_{corr} against $h\nu$ dependence [53, 54]:

$$\alpha = \frac{\alpha_1}{1 + \exp\left(\frac{E_U - h\nu}{E_0}\right)} \tag{4}$$

where α_1 is a constant absorption and E_{U} is another energy parameter (Urbach focus) that can be assimilated to the bandgap energy [21]. This curve tends to equation (3) in the limit $h\nu \ll E_{\mathrm{U}}$, with $\alpha_0 = \alpha_1 \exp(-E_{\mathrm{U}}/E_0)$, but saturates at the limiting value α_1 as $h\nu \gg E_{\mathrm{U}}$. Therefore, it automatically generates the inflection needed for further direct band absorption. Figure 7 shows the corresponding fittings for the ED series whose E_{02} values extracted from equation (4) are shown in table 2(b).

Both processes for finding E_0 give close-by values that correlate well with the E_{g} obtained for these samples. This suggests that the bandgap energy shift, originated in the free

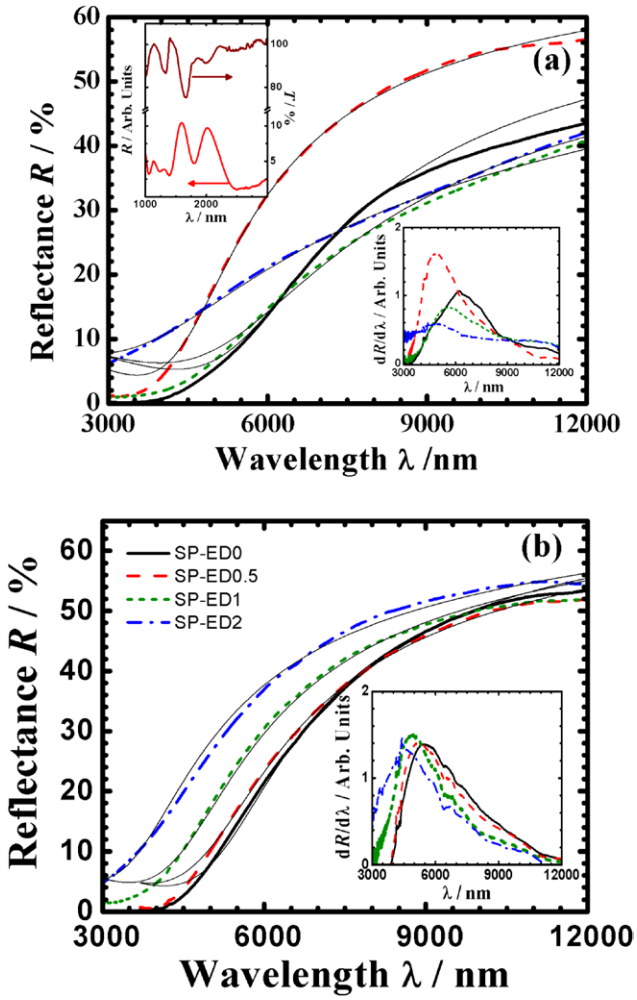

Figure 8. Infrared reflectance for the same samples as in figure 4: (a) ED series, (b) SP-ED series. Thin lines correspond to fitting according to the Drude model. Lower insets correspond to the first derivative of measured spectra. Upper inset in (a) is diffuse reflectance and transmittance for sample ED0.5 in the near infrared.

carriers through Moss–Burstein effects, may be due to the incorporation of defects (probably chloride impurities). That means the Cl doping is effectively incorporating (extrinsic or intrinsic) defects into the ZnO lattice, which generates lattice imperfections increasing the E_0 Urbach's parameter. Theoretical calculations suggest that Cl^- may not generate shallow donor states, but unintentional hydrogen co-doping may be responsible for the free carriers [55]. In contrast, more recent calculations do suggest that Cl^- acts as a donor state [56]. Other authors suggest Cl contributes to the formation of Zn interstitials that are well known donor states in ZnO [57]. In any case, it is clear there is a direct correlation between the Cl^-/Zn^{2+} ratios and the free carriers that influence the optical and electrical properties.

For further verification of the presence of free carriers (electrons), the infrared optical properties were also studied [10, 42, 56]. Lindgren *et al* [58] have recently listed the methods used to determine carrier concentrations in semiconductor nanowires. Many of them require the use of single nanowire structures, while others, like electrochemical impedance spectroscopy (EIS) [57, 59, 60], may be applied to nanopillar arrays. However, optical characterization has the advantage of requiring no electrical contact [58].

Figure 8 shows the reflectance spectra in the region from 3–12 μm for the ED series (figure 8(a)) and SP-ED series (figure 8(b)), where a rapid increase in the reflectance response indicates a metallic-like behaviour [61]. For larger wavelengths (region not shown) the spectra have a clear characteristic of ZnO phonon resonance at $\sim$17 μm [62, 63]. For shorter wavelengths, the spectra show oscillations in reflectance and transmittance, as shown in figure 8(a) upper inset for sample ED0.5. Note that each maximum (minimum) in the transmittance has a corresponding minimum (maximum) in the reflectance. From these oscillations, effective thicknesses between 1600–1800 nm were estimated using a refraction index $n_{ZnO} \sim 2$ [4].

The shifts in the spectra of figure 8 are directly related to the free electron densities. Similar shifts in the transmittance spectra to higher energies with increasing chloride contents have been observed before for ZnO thin films [10].

The estimation of free electron densities from the reflectance data can be obtained using [29]:

$$R = \left| \frac{\sqrt{\varepsilon_r} - 1}{\sqrt{\varepsilon_r} + 1} \right|^2 \tag{5}$$

where ε_r is the dielectric constant obtained by the Drude model:

$$\varepsilon_r = \varepsilon_{opt}\left(1 - \frac{\omega_p^2}{\omega^2 + i\gamma\omega}\right) \tag{6}$$

In the expression $\omega = 2\pi c/\lambda$, $\varepsilon_{opt} = n_{ZnO}^2 \sim 4$ is the dielectric constant in the transparent region, γ is the damping rate and ω_p is the plasma frequency, which depends on the free electron density n as:

$$\omega_p^2 = \frac{ne^2}{\varepsilon_{opt}\varepsilon_0 m_e} \tag{7}$$

where e is the electron charge and ε_0 is vacuum electrical permittivity.

Different methods were used for obtaining the densities n from ω_p. In the first place, the plasma frequency was estimated from the maximum of the derivative of the reflectance spectra (see figures 8(a) and (b) lower insets). This approximation is accurate for small damping rates, but is an underestimation of the actual ω_p. In the second place, equations (5) and (6) were used to fit the reflectance spectra using ω_p and γ as fitting parameters. The thin full lines in figure 8 show the best fittings for each sample. Moreover, it can be seen how the onset of reflectance shifts to the visible region with the Cl^-/Zn^{2+} ratio. This is another suggestion that Cl doping is effectively incorporating defect states into the ZnO lattice and generating free carriers in the semiconductor.

To avoid the influence of events in the spectra that may be detrimental in the fitting method (interference and absorption previously mentioned) a third method was used in which ω_p and γ were both obtained from the maximum of the reflectance first derivative ω_{max} and its full width at half maximum

ω_{FWHM}. From equations (5) and (6) a system of two equations can be numerically found that determines uniquely ω_p and γ from ω_{max} and ω_{FWHM} (or their corresponding values in wavelength).

Table 2(a) shows the resulting ω_p calculated as the average of the values obtained by the three methods and its uncertainty was estimated as the maximum of the differences of the average and the estimated values. An analogue procedure was applied to obtain γ from the last two methods. Finally, a free electron density n_3 can be calculated using equation (7) as shown in table 2(a). The results are mainly affected by the ZnO parameters used in equations (6) and (7) such as ε_{opt} and m_e, where we have used the ones usually reported for bulk ZnO. The electron effective mass m_e is not expected to change because, as previously mentioned, no quantum confinement is present. The dielectric constant may be affected by the porosity of the nanostructures [37], especially for the lowest diameter nanopillars. However, ZnO having a relatively low refractive index, in comparison with other binary semiconductors, the correction will not change the order of magnitude of the results. Otherwise, light scattering, especially for thicker nanopillars, may affect the reflectance of equation (5). But it is well known that the diffuse contribution to the reflectance decreases into the infrared region [10, 11, 25, 30]. In effect, for the present results, other fitting processes were tried adding a constant reflectance in equation (5) as a way of including diffused contribution in a first approximation, but the best fittings were those in figure 8.The results in table 2 compare well with values of carrier concentrations calculated from Mott–Schottky plots by other authors. Rousset *et al*[10] report that the carrier concentration for ZnO films is enhanced by the increase of the chlorides in the electrodeposition bath, reaching 9×10^{19} cm^{-3} for $[Cl^-] = 0.1$ mol l^{-1}, which seems to be close to the maximum reachable carrier concentration. For electrodeposited nanowires, Tena-Zaera *et al* [57] used an extended Mott–Schottky equation for cylindrical geometry to calculate the donor density of ZnO nanowires and reported values from slightly lower than 10^{19} cm^{-3} to higher than 10^{20} cm^{-3} as a function of KCl concentration.

As the ω_p increases, as a general rule, with the Cl^-/Zn^{2+} increase, the density n_3 also increases. For the samples of the ED series these densities have the same tendencies as the ones shown in table 1 and values quite similar to the n_2 column in that table. As these values were greatly influenced by the $E_g(0)$ parameter, the agreement between them is relatively good. Note that the n_2 values were obtained with a more acceptable value of $E_g(0) = 3.30$ eV [64] for undoped ZnO than the n_1 values. For the SP-ED series the n_3 values monotonically increase with Cl^-/Zn^{2+} and are in the same order as the ED series. In fact, if the uncertainties are taken into consideration, the n_3 intervals for each Cl^-/Zn^{2+} value overlap for both the ED and SP-ED series. This happens even for ED1 and SP-ED1, considering that ED1 seems to move away from this tendency. But this is because the ED1 samples showed the greater relative dispersion in all measurements. Therefore, although the values obtained by the Moss–Burstein method were quantitatively lower for the SP-ED series—because the absorption edge of the compact layer is dominating the optical measurements and does not allow us to observe the shifts of the electrodeposited nanostructures onto it—these samples are also being effectively doped by the Cl content, as was previously observed by the electrical properties.

Finally, it is very important to note from table 2(a), that in all samples the damping rate γ increases with the Cl^-/Zn^{2+} ratio. As this parameter measures the collision rate of the free electrons inside the crystalline ZnO, it indicates that more collisional centres are present as Cl^-/Zn^{2+} increases. As defect states act as collisional centres, this may be an indication that Cl impurities are being properly incorporated into the ZnO lattice, as also previously observed from the Urbach parameter. However, some authors suggest that Cl act as an indirect doping agent, which contributes to the formation of intrinsic defect sates rather than as an extrinsic dopant [30, 57].

4. Conclusions

Nanopillars of Cl-doped ZnO were grown by electrodeposition onto bare FTO/glass and ZnO-compact layer/FTO/glass substrates. The Cl^-/Zn^{2+} ratios in the nanostructured films, measured by EDS, correlate well with the Cl^-/Zn^{2+} ratio in solution. This ratio affects not only the morphology of the nanopillars but their structural, electrical and optical properties. In fact, the electrical resistance (measured by 4-point in-line method and 1-point Schottky barrier contact) diminishes with increasing Cl doping. The UV optical absorption edge (ZnO bandgap energy) shifts to upper energy with doping due to the Moss–Burstein effect, which corresponds to electron densities in the order of 1–6 $\times$ 10^{19} cm^{-3}. The infrared spectra also reveal the presence of free electrons and a corresponding shift to higher energy, allowing a more precise determination of the free electron densities. Moreover, the damping rate obtained from infrared measurements and the Urbach tail parameter from below gap UV absorption both show that chloride acts as a dopant inside ZnO crystal structure.

Acknowledgments

CONICET-ANII Project MOV_CO_2013_1_100005 and ANPCyT Project PICT 993/13 supported this work. The authors acknowledge the financial support received from the Consejo Nacional de Investigaciones Científicas y Técnicas (CONICET) and Universidad Nacional de Mar del Plata, both from Argentina. DLG, EAD and REM also acknowledge support from ANII (Agencia Nacional de Investigación e Innovación) Project FSE_1_2014_1_102184, CSIC and PEDECIBA—Física, Uruguay. Thanks also to S Botasini and E Méndez for allowing the use of FTIR.

References

[1] Yu R, Lin Q, Leung S-F and Fan Z 2012 *Nano Energy* **1** 57–72
[2] Schmidt-Mende L and MacManus-Driscoll J L 2007 *Mater. Today* **10** 40–8
[3] Janotti A and Van de Walle C G 2009 *Rep. Prog. Phys.* **72** 126501

[4] Norton D P, Heo Y W, Ivill M P, Ip K, Pearton S J, Chisholm M F and Steiner T 2004 *Mater. Today* **7** 34–40
[5] Duan H, He H, Sun L, Song S and Ye Z 2013 *Nanoscale Res. Lett.* **8** 1–6
[6] Kato H, Sano M, Miyamoto K and Yao T 2002 *J. Cryst. Growth* **237–9** 538–43
[7] Kim H, Horwitz J S, Qadri S B and Chrisey D B 2002 *Thin Solid Films* **420–1** 107–11
[8] Yousefi R and Kamaluddin B 2009 *Appl. Surf. Sci.* **255** 9376–80
[9] Guillén-Santiago A, Olvera M D L L, Maldonado A, Asomoza R and Acosta D R 2004 *Phys. Status Solidi a* **201** 952–9
[10] Rousset J, Saucedo E and Lincot D 2009 *Chem. Mater.* **21** 534–40
[11] Tena-Zaera R, Elias J and Lévy-Clément C 2008 *Appl. Phys. Lett.* **93** 233119
[12] Park J-H, Lee T I, Hwang S-H, Moon K-J and Myoung J-M 2015 *Prog. Photovolt., Res. Appl.* **23** 813–20
[13] Cembrero-Coca P, Mollar M, Singh K C and Marí B 2013 *ECS J. Solid State Sci. Technol.* **2** Q108–12
[14] Öztürk S, Kılınç N, Taşaltin N and Öztürk Z Z 2011 *Thin Solid Films* **520** 932–8
[15] Fan J *et al* 2011 *Acta Mater.* **59** 6790–800
[16] O'Regan B, Schwartz D T, Zakeeruddin S M and Grätzel M 2000 *Adv. Mater.* **12** 1263–7
[17] Elias J, Tena-Zaera R and Lévy-Clément C 2007 *Thin Solid Films* **515** 8553–57
[18] Smits F M 1958 *Bell Syst. Tech. J.* **37** 711–8
[19] Han X, Han K and Tao M 2010 *J. Electrochem. Soc.* **157** H593–7
[20] Henríquez R, Grez P, Muñoz E, Gómez H, Badán J A, Marotti R E and Dalchiele E A 2010 *Thin Solid Films* **518** 1774–8
[21] Johnson S and Tiedje T 1995 *J. Appl. Phys.* **78** 5609–13
[22] Marotti R E, Badán J A, Quagliata E and Dalchiele E A 2007 *Physica* B **398** 337–40
[23] Cui J B, Soo Y C, Chen T P and Gibson U J 2008 *J. Phys. Chem.* C **112** 4475–9
[24] Cullity B D 1978 *Elements of X-Ray Diffraction* (Reading, MA: Addison Wesley)
[25] Pereyra C J *et al* 2013 *Energy Environm. Focus* **2** 257–69
[26] Bojorge C D, Kent V R, Teliz E, Cánepa H R, Henríquez R, Gómez H, Marotti R E and Dalchiele E A 2011 *Phys. Status Solidi a* **208** 1662–9
[27] Marotti R E, Bojorge C D, Broitman E, Cánepa H R, Badán J A, Dalchiele E A and Gellman A J 2008 *Thin Solid Films* **517** 1077–80
[28] Znaidi L, Soler Illia G J A A, Benyahia S, Sanchez C and Kanaev A V 2003 *Thin Solid Films* **428** 257–62
[29] Pauporte T and Lincot D 2000 *Electrochim. Acta* **45** 3345–53
[30] Tena-Zaera R, Elias J, Wang G and Lévy-Clément C 2007 *J. Phys. Chem.* C **111** 16706–11
[31] Leung S-F, Zhang Q, Xiu F, Yu D, Ho J C, Li D and Fan Z 2014 *J. Phys. Chem. Lett.* **5** 1479–95
[32] Musselman K P, Wisnet A, Iza D C, Hesse H C, Scheu C, MacManus-Driscoll J L and Schmidt-Mende L 2010 *Adv. Mater.* **22** E254–8
[33] Nowak R-E, Vehse M, Sergeev O, von Maydell K and Agert C 2014 *Sol. Energy Mater. Sol. Cells* **125** 305–9
[34] Badán J A, Marotti R E, Dalchiele E A, Ariosa D, Martín F, Leinen D, Ochoa E and Ramos-Barrado J R 2015 *J. Mater. Res.* **30** 753–60
[35] Pankove J 1971 *Optical Processes in Semiconductors* (New York: Dover)
[36] Sapoval B and Hermann C 1993 *Physics of Semiconductors* (New York: Springer)
[37] Stenzel O 2005 *The Physics of Thin Films Optical Spectra: an Introduction* (Berlin: Springer)
[38] Tauc J 1970 *Mater. Res. Bull.* **5** 721–9
[39] Bojorge C D, Cánepa H R, Gilabert U E, Silva D, Dalchiele E A and Marotti R E 2007 *J. Mater. Sci., Mater. Electron.* **18** 1119–25
[40] Sernelius B E, Berggren K F, Jin Z C, Hamberg I and Granqvist C G 1988 *Phys. Rev.* B **37** 10244–8
[41] Burstein E 1954 *Phys. Rev.* **93** 632–3
[42] Chikoidze E, Nolan M, Modreanu M, Sallet V and Galtier P 2008 *Thin Solid Films* **516** 8146–9
[43] Marotti R E, Guerra D N, Bello C, Machado G and Dalchiele E A 2004 *Sol. Energy Mater. Sol. Cells* **82** 85–103
[44] Riveros G, Gomez H, Henríquez R, Sshrebler R, Córdova R, Marotti R E and Dalchiele E A 2002 *Bol. Soc. Chilena Quím.* **47** 411–29
[45] Lee J, Park E, Subramaniam N G, Lee J, Lee J, Lee J and Kang T 2012 *Curr. Appl. Phys.* **12** S80–4
[46] Grundmann M 2006 *The Physics of Semiconductors: an Introduction Including Devices and Nanophysics* (Berlin: Springer)
[47] Button K J, Cohn D R, von Ortenbert M, Lax B, Mollwo E and Helbig R 1972 *Phys. Rev. Lett.* **28** 1637–9
[48] Hümmer K 1973 *Phys. Status Solidi* b **56** 249–60
[49] Roth A P, Webb J B and Williams D F 1982 *Phys. Rev.* B **25** 7836–9
[50] Tiburcio-Silver A, Joubert J C and Labeau M 1994 *J. Appl. Phys.* **76** 1992–4
[51] Urbach F 1953 *Phys. Rev.* **92** 1324
[52] Srikant V and Clarke D R 1997 *J. Appl. Phys.* **81** 6357–64
[53] He H P, Zhuge F, Ye Z Z, Zhu L P, Wang F Z, Zhao B H and Huang J Y 2006 *J. Appl. Phys.* **99** 023503
[54] Martin R, Middleton P, O'Donnell K and Van der Stricht W 1999 *Appl. Phys. Lett.* **74** 263–5
[55] Liu B, Gu M, Liu X, Huang S and Ni C 2013 *Solid State Commun.* **171** 30–3
[56] Tsin F *et al* 2015 *Sci. Rep.* **5** 8961
[57] Tena-Zaera R, Elias J, Lévy-Clément C, Bekeny C, Voss T, Mora-Seró I and Bisquert J 2008 *J. Phys. Chem.* C **112** 16318–23
[58] Lindgren D, Hultin O, Heurlin M, Storm K, T. Borgström M, Samuelson L and Gustafsson A 2015 *Nanotechnology* **26** 045705
[59] Mora-Seró I, Fabregat-Santiago F, Denier B, Bisquert J, Tena-Zaera R, Elias J and Lévy-Clément C 2006 *Appl. Phys. Lett.* **89** 203117
[60] Tena-Zaera R, Elias J, Lévy-Clément C, Mora-Seró I, Luo Y and Bisquert J 2008 *Phys. Status Solidi a* **205** 2345–50
[61] Fox A M 2001 *Optical Properties of Solids* (Oxford: Oxford University Press)
[62] Bundesmann C, Schmidt-Grund R and Schubert M 2008 Optical properties of ZnO and related compounds *Transparent Conductive Zinc Oxide: Basics and Applications in Thin Film Solar Cells* ed K Ellmer *et al* (Berlin: Springer) pp 79–124
[63] Madelung O 2012 *Semiconductors: Data Handbook* (Berlin: Springer)
[64] Özgür Ü, Alivov Y I, Liu C, Teke A, Reshchikov M, Doğan S, Avrutin V, Cho S-J and Morkoc H 2005 *J. Appl. Phys.* **98** 041301